

# Tuning and Modulation of the Photoinduced Current by Rectification of Surface Plasmons in Metal–Molecule–Nanoparticle–ITO Composite Junctions

Published as part of *The Journal of Physical Chemistry C virtual special issue "Hiroaki Misawa Festschrift."*

Maoning Wang, Valentin Barth, Sergii Snegir, Lukas Holz, Thomas Huhn, Johannes Boneberg, Chenyang Guo, Mengqi Fu, Dong Xiang,\* Paul Leiderer, Fan Yang,\* and Elke Scheer\*



Cite This: *J. Phys. Chem. C* 2024, 128, 8315–8323



Read Online

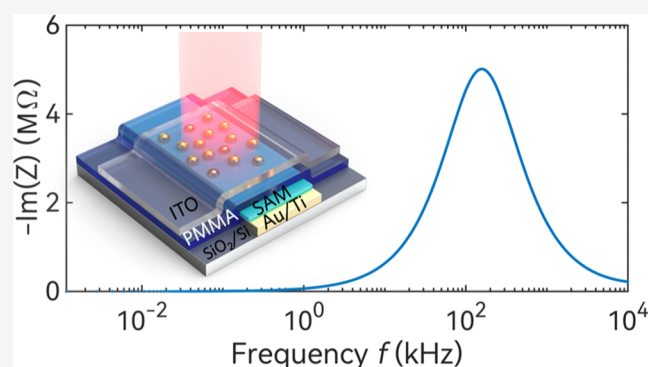
ACCESS |

Metrics & More

Article Recommendations

Supporting Information

**ABSTRACT:** Au nanoparticles (AuNPs) are prime candidates to build up device components for light-harvesting and photon–electron conversion. AuNPs respond to light irradiation by creating localized surface plasmons (LSPs), coupling with neighboring AuNPs and the substrate, to generate intense fields. Here, we present a novel optoelectronic multilayer heterostructure to transmit the LSP response directly into alternating current (AC) on the tens of nanoampere level under modulated laser illumination in the hundred kilohertz range. The device is composed of a metal bottom layer, a self-assembled molecular monolayer (SAM), AuNPs, and indium tin oxide (ITO) as the transparent top layer. We show that ITO is a suitable material for the top electrode of the device because of its higher optical transparency for a given thickness, and we discuss the optoelectronic properties of the heterostructure. Furthermore, we show that the AC response can be tuned by a direct current (DC) bias, the illumination power, and wavelength, and we study the position dependencies of the LSP signal, thereby illustrating the multiple controllability of the heterostructure device. The investigation presents a novel device concept and contributes to future nanoscale applications in fundamental research, sensing, and energy harvesting based on the AC optoelectronic response. The novel design of the heterostructure could also lead to possible approaches for AC optoelectronic converter applications.



## INTRODUCTION

By producing an intense and highly localized electromagnetic field, localized surface plasmons (LSPs) can amplify electrical charge transport in devices where the incident light triggers LSPs in nanogap antennas.<sup>1,2</sup> Nanogap antennas in various realizations have attracted high interest in recent years to confine light, harvest energy, and produce photoinduced current. Adaptable functionalities with corresponding LSP-based structures encompass a broad range of applications, such as surface-enhanced sensing,<sup>3</sup> nanolight sources,<sup>4</sup> molecular trapping,<sup>5</sup> and optoelectronic switches.<sup>6</sup> The illuminating electromagnetic field in nanoparticle (NP)-based antennas is enhanced in gaps and junctions between the NPs and induces LSP oscillations, which represent alternating LSP currents. These alternating LSP current signals could be converted to voltage signals when the antennas are electrically contacted and embedded in electrical circuits and can thus be collected and analyzed, e.g., by lock-in amplification taking advantage of the rectification due to nonlinearities of the current–voltage characteristics.<sup>7</sup> As shown already in Möller et al.,<sup>7</sup> the

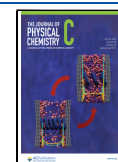
activation of plasmons may result in a direct current (DC) current due to a pronounced enhancement of the electric field. The rectification is proportional to the curvature of the current–voltage characteristics ( $I_{dc}$ – $V_{dc}$ ). Hence, junctions with designed electronic transport properties in combination with a high plasmon excitation efficiency are beneficial for applications based on this mechanism. The most common nanostructures to achieve nanogap antennas include, among others, metallic dimers, bowtie nanogaps, break junctions, and nanoparticle-on-mirror (NPOM) configurations.<sup>8</sup> Considerable efforts have been put into the integration and fabrication of plasmonic antennas with current-carrying nanoelectronic

Received: March 15, 2024

Revised: April 23, 2024

Accepted: April 25, 2024

Published: May 8, 2024



devices.<sup>8</sup> They offer great prospects toward opto-plasmonic nanocircuits using near-field coupling, and the basic plasmonic components provide modulation ability of both optical and electric properties. However, this approach bears many challenges, especially the integration challenge and parameter matching to make individual nanoplasmonic devices compatible with external electric circuits. To date, direct nanometer-dimension electrical detection of confined optical LSPs from metallic nanostructures alone is still limited to special situations, incapable of expanding into universal device applications.<sup>9,10</sup>

Among the common nanostructures, the NPoM configuration has advantages in its relative ease of fabrication by a bottom-up assembly process and clearer plasmon mode analysis because of the symmetry introduced by the flat metal mirror. It also has superior advantages of being modified into optoelectronic circuits by introducing an insulating interlayer and top electrodes. Very recently, Baumberg and co-workers reported a novel kind of molecular junction based on the NPoM configuration.<sup>10</sup> The self-assembled molecular monolayer (SAM) is placed between the NP and the underlying flat gold surface, where the molecular junction is electrically contacted and optically accessible. The functions are achieved by coating a poly(methyl methacrylate) (PMMA) layer, then reducing the PMMA layer thickness by dry etching, and finally depositing the top gold electrodes. This seminal concept is promising, but there are still aspects left to solve. For example, the NP density was chosen to be quite low to study the response of an individual NP, and the laser light was strongly focused onto the NP area to achieve the necessary optical intensity to achieve a measurable signal. Furthermore, operating under a microscope is not practical for many applications. The influence of the NP density on the device functionalities and operational capability has not been explored yet. The transmittance of light is rapidly reduced as the thickness of the gold top layer increases.<sup>11</sup> The decrease of the light transmittance may result in increased light scattering between neighboring NPs thereby effectively diffusing the illumination of the individual particles.<sup>11,12</sup> Besides, it cannot be excluded that the light reflection or the light scattering from the ultrathin upper gold layer would also contribute to the response signal collected by the electrical circuits, especially when its thickness is in the same order as the NP size.<sup>13</sup> Recently, the well-known indium tin oxide (ITO) came into focus as an electrode material in optoelectronic devices because of its combination of sufficient electrical conductivity, optical transparency, and favorable adhesion to polymer film surfaces and the possibility of film deposition for the desired microscopic structure.<sup>14–17</sup> A compromise must be made between electrical conductivity and optical transparency since increasing the film thickness and the concentration of charge carriers correspondingly increases the film's conductivity but decreases its transparency.<sup>18</sup> Here, we design a device that operates on the same principle as reported in ref 10, but that is improved regarding the electrode material and the cross section to achieve sufficient signal size without extreme focusing and to make the devices suitable for medium frequency operation in the hundreds of kHz to MHz regime.

Here, we demonstrate a novel approach toward achieving long-lived microscale junctions combining nano-optical and nanoelectrical aspects. The core idea is to design and fabricate the upper electrode by polycrystalline ITO to fulfill the double purpose of effectively transmitting the illuminating

light to the junction area and simultaneously serving as an electrical contact. We achieved a design using arrays of junctions on one single substrate allowing for parameter variation and future optically accessible and displaying applications. DC and AC techniques are utilized to characterize the LSP effects and their bias-tuning properties by measuring photoinduced current responses of the junction. Furthermore, we discuss the optoelectroconductive microscopic mechanism of the optimized junction for LSP characterization.

## METHODS

**Sample Fabrication.** All of the samples have been fabricated on Si wafers with a 300 nm thick SiO<sub>2</sub> layer on top (Si-Mat). The bottom electrodes are fabricated by thermal evaporation (NanoPVD-T15A, Moorfield Nanotechnology) of 5 nm Ti as an adhesion layer and then 100 nm of Au at a rate of 0.5 nm/s through the designed shadow masks (Rigorous Technology). The formation of a 1.64 nm thick SAM is achieved by first producing a mixture of 1,10-decanedithiol and 9-mercapto-1-nonanol (Sigma-Aldrich) with a ratio of 1:1. The mixture of the two molecules is chosen to reduce the formation of disulfide bonds so that the SAM functions as both electrical components and a spacer layer with fixed thickness.<sup>19–21</sup> Next, the sample is placed overnight into a 1 mM solution of the mixed molecules dissolved in 99.9% ethanol, then washed with ethanol, and blown dry with nitrogen. AuNPs with diameters of 30 nm (BBI solutions) are self-assembled on prepared samples with a deposition time of 2 min and then blown dry with nitrogen. For one sample, the deposition time was increased to 1 h to induce NP aggregation. In other samples, NPs with 60 nm diameter were used instead, while all other fabrication processes were identical. Poly(methyl methacrylate) (PMMA A2; MicroChem) at 2 wt % (molecular weight, 950 kg/mol) was dissolved in anisole. The PMMA was spin-coated at a speed of 6000 and 2500 rpm/s acceleration for 1 min and subsequently baked at 50 °C on a hot plate for 4 min. The final PMMA thickness on the SiO<sub>2</sub> surface is ~67 nm. Partially embedded 30 (60) nm AuNPs are obtained by removing 45 (30) nm of the PMMA layer using dry etching in an oxygen plasma (Oxford Instruments, PlasmaPro 80 Cobra), leaving the top part of the NPs exposed for contact formation with the upper electrode. The intermediate PMMA layer effectively prevents the parasitic current between the electrodes and the NPs. For the upper electrode, 100 nm of ITO was sputtered through a designed shadow mask. The material composition of ITO is 90% In<sub>2</sub>O<sub>3</sub> and 10% SnO<sub>2</sub>. For the reference sample shown in Figure S3a–c, a 4 nm thin Au layer was thermally evaporated instead to form the top electrode. Notably, to avoid thermal harm to the underneath SAM, neither the junctions with ITO nor those with Au as the top electrode were annealed during the fabrication process. The film thickness of each sample was characterized by ellipsometry (Sentech Instruments GmbH) and profilometry (DektakXT) before and after plasma etching.

**Electrical Measurements.** The two electrodes on each sample are contacted electrically with tungsten probes (LakeShore) mounted in a custom multiple terminal probe station. All electrical measurements are performed at room temperature and ambient conditions. The probes are connected to a lock-in amplifier (LIA, HF2LI, Zurich Instruments) for the alternating current (AC) or a semiconductor analyzer (4156C, Agilent) for the direct current

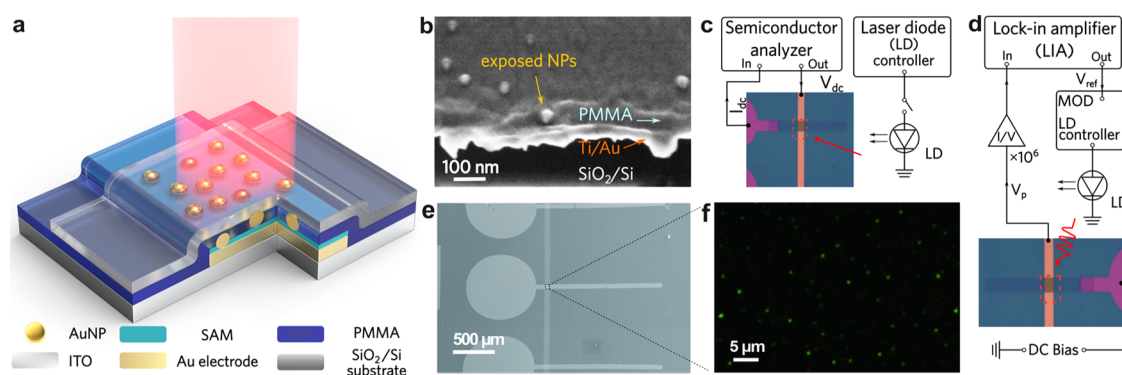


**Figure 1.** Device geometry and measurement circuit. (a) Scheme of the layered device structure of the MeMoNPI junctions. (b) Cross-sectional SEM image of a sample without a top electrode. The sample was broken across the bottom electrode. It reveals that the AuNPs are partially embedded into PMMA and partially exposed to the environment after oxygen plasma etching. (c) DC ( $V_{dc}$ ) measurement scheme using the semiconductor analyzer and illumination with constant intensity. (d) AC measurement scheme using lock-in technique and illumination with AC modulated intensity.  $V_{ref} = V_{mod} \sin(2\pi f_{mod} t)$  is the voltage sent into the LD controller to modulate the laser intensity, where  $f_{mod}$  is the modulation frequency, set as 160 kHz unless otherwise stated. The optical micrographs in (c, d) show a single crossbar junction with a 4 nm Au top layer at the junction area and 30 nm thick gold contact pads as an example to demonstrate the connection with the measurement circuits. (e) SEM top view image of junctions with a 100 nm thick ITO top electrode (horizontal stripes with circular contact pads left) and a 100 nm Au bottom electrode (vertical stripe). (f) Dark-field image of the area marked in (e). The green spots indicate AuNPs with diameters of approximately 30 nm.

(DC) measurements. The bottom electrode is connected to a current/voltage converter with a factor of  $10^6$  A/V amplification, while the upper electrode is connected directly to the DC voltage source. DC current–voltage ( $I_{dc}$ – $V_{dc}$ ) curves are recorded with the semiconductor analyzer. The AC response of the junctions to frequency-modulated light is acquired by the LIA, with the same frequency with which the laser light source is modulated. In our work, we set the frequency to 160 kHz. We also tested lower and higher frequencies and found qualitatively similar but quantitatively different signals. An example of a frequency dependence for otherwise fixed parameters is shown in Figure S8. A DC offset from  $-5$  to  $5$  V can be added to the junctions by the LIA.

**Optical Setup.** A 633 nm laser diode (ITC 502, Thorlabs) is controlled by an LD controller (Thorlabs) to adjust the laser power. Several mirrors introduce the laser into the chamber of the probe to illuminate the junction. The laser beam is always kept at normal incidence. The output port of the LIA also functions as a reference to provide a frequency signal for the LD controller. The modulation frequency is set to 160 kHz. For the control measurement with and without illumination, a shutter was used to permit or hinder the light. The switching speed of the shutter was set to 0.05 Hz. Other light wavelengths were realized by replacing the LD with LDs with wavelengths 440, 532, and 980 nm, respectively, using the same LD controller. The value of the laser power was measured with a power meter (S120C, Thorlabs) at the sample location.

## RESULTS AND DISCUSSION

Combining the above considerations, the final junction geometry is designed to be a layered heterostructure composed of a metal bottom electrode, SAM–AuNPs–ITO, which we label as a MeMoNPI junction (Figure 1a). To achieve that, we first deposit a  $150 \mu\text{m}$  wide  $50 \text{ nm}$  thick gold stripe on the bottom silicon substrate ( $500 \mu\text{m}$  Si covered with  $300 \text{ nm}$   $\text{SiO}_2$ ) and then introduce a  $1.64 \text{ nm}$  thick SAM (a mixture of 1,10-decanedithiol and 9-mercapto-1-nonanol with the ratio of 1:1) featuring chemical anchors on both ends. The SAM material is chosen to form a uniform and defect-free molecular

layer that provides a certain resistance and nonlinear current–voltage characteristics. Choosing another molecular system might change the quantitative response but not the qualitative response of the devices as long as it has no particular photochromic properties. Next, we integrate citrate-stabilized AuNPs with diameters of 30 or 60 nm on top of the SAM layer. Next, PMMA insulating layer is deposited for encapsulation, and its thickness is reduced by dry etching such that the upper calotte of the AuNPs is freed (Figure 1b). Finally,  $100 \text{ nm}$  ITO (or for the reference sample:  $4 \text{ nm}$  Au) is added as a top electrode to form crossbar junctions.<sup>22</sup> The upper electrode thickness was designed to guarantee at least 79% transmission in the visible light range.<sup>23</sup> To protect the SAMs underneath the NPs, we avoid thermal processing after the deposition of the top electrode so that the device's DC resistance is not further reduced and falls within a range of  $10^7$ – $10^9 \Omega$ . From the geometrical and material properties, it can be estimated that the AC resistance of the device in the hundred kHz range is about 2 orders of magnitude smaller. One individual sample contains arrays of approximately 90 crossbar junctions, and the scanning electron microscope (SEM) image in Figure 1e shows an example of a MeMoNPI junction with an area of  $150 \mu\text{m} \times 150 \mu\text{m} = 22500 \mu\text{m}^2$ . Neglecting aggregation effects, we estimate a particle density of  $76 \text{ NPs}/\mu\text{m}^2$  on average [see Figure S1 in the Supporting Information (SI)]. In view of this density and taking into account possible aggregation at some positions in the junctions, both near-field and far-field interactions may come into play. These junctions are electrically characterized by contacting the bottom and the top electrodes via two tip probes inside a probe station under an air atmosphere at room temperature. The probes are connected to a semiconductor analyzer or an LIA for recording the DC or AC signals, respectively, see Figure 1c,d. The laser beam is focused and always in normal incidence; the experiments were performed with a wavelength of 633 nm unless stated otherwise.

As indicated before, we replaced the usual Au top electrode with a  $100 \text{ nm}$  thick ITO layer that has a typical optical transmittance of  $\sim 80\%$ .<sup>10,23</sup> This is done to avoid artifacts that were observed in junctions with a  $4 \text{ nm}$  thin Au top layer and

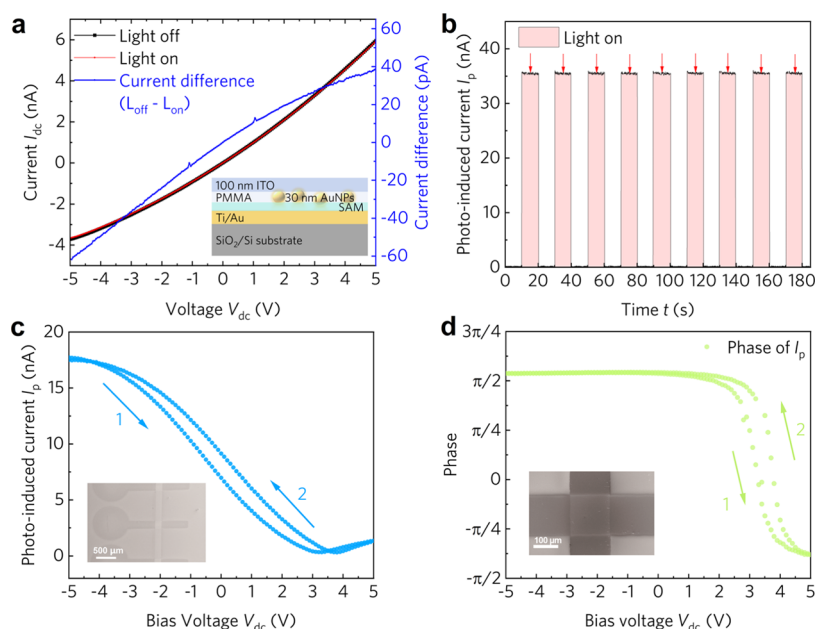


**Figure 2.**  $I_{dc}$ – $V_{dc}$  curves and photoinduced current response of sine-modulated laser illumination of a MeMoNPI junction. The laser wavelength is 633 nm, and the power is  $\sim 120 \mu\text{W}$  (unfocused to cover one entire junction, with a light spot size of  $\sim 1.2$  mm). When measuring  $I_{dc}$  and  $V_{dc}$ , the laser intensity is set to constant without any modulation. The average NP diameter inside the junction is 30 nm. (a)  $I_{dc}$ – $V_{dc}$  curves in dark (black line) or under continuous illumination (red line) measured by the semiconductor analyzer. The black and red curves fall almost on top of each other. The blue curve represents the difference between the black and the red line and refers to the right axis. A scheme of the cross section of the MeMoNPI junction is shown in the inset. (b) Photoinduced current response measured by LIA while the shutter in the optical path is periodically switched between on or off with a frequency of 0.05 Hz. The modulation frequency of the laser intensity is set to 160 kHz and is always on. The red-shaded area corresponds to the shutter being open, i.e., illuminating the junction. (c) Photoinduced current vs DC offsets of the MeMoNPI junction. Here, the photoinduced current is measured by LIA while a varying DC bias voltage is applied to the top and bottom electrodes, shown as inset. The arrows and numbers indicate the sweep direction. (d) Corresponding measured phase with respect to (c) by LIA measurements. A blow-up of the crossbar area of the junction is shown as inset.

that were of the same order and similar type as the ones expected from the NPs. Although the origin of these artifacts could not be clearly revealed, we attribute them to the granular structure of the film; see SI, Figure S2 for control experiments. Increasing the thickness can reduce the granularity of the top electrode but also reduce its optical transparency. Selective angle incidence might be a solution for compensation but is inefficient for large-scale junctions. The ITO electrode is not only optically transparent, but it also provides a capacitance that defines the AC resistance,<sup>24</sup> such that an equivalent resistor–capacitor (RC) circuit is built, see Figure S1g. The RC character of the ITO together with the stray capacitance of the embedding circuit defines a frequency range in which the AC signal adopts a maximum. The modulation frequency was chosen in this frequency range.

At first, we measure the DC current–voltage ( $I_{dc}$ – $V_{dc}$ ) characteristics of the junctions, both in the dark and under continuous laser illumination with a laser power of 120  $\mu\text{W}$  (unfocused—with a spot diameter of  $\sim 1.2$  mm and hence a light intensity of  $\sim 15 \text{ mW}/\text{cm}^2$ —to cover one entire junction) using the semiconductor analyzer. As shown in Figure 2a, the overall shape of the  $I_{dc}$ – $V_{dc}$  of one MeMoNPI junction both with and without illumination is slightly nonlinear and asymmetric, as typical for multimolecule junctions of species with large HOMO–LUMO (HOMO: highest occupied molecular orbital, LUMO: lowest unoccupied molecular orbital) gap with two different electrode materials.<sup>25</sup> Another possible resistance contribution arises from the contact resistance between the AuNPs and the electrodes. To characterize the electronic transport properties of the SAM

independently, we utilized the scanning tunneling microscope break junction (STM-BJ) method. In the SI (Figure S4), the statistical conductance of 1,10-decanedithiol single-molecule junctions is shown. From these experiments, we conclude that the SAM indeed separates the AuNPs from the bottom electrode at the position where we apply the STM tip. While the contact between the bottom electrode and the NPs is controlled by the properties of the SAM, the contact to the top electrode may vary depending on whether a PMMA layer remains on top of the NPs after etching. The DC resistance of most junctions including the SAM, PMMA, and AuNPs is in the order of 1 G $\Omega$  and hence about 2 orders of magnitude larger than that of a sandwich of an Au bottom electrode and bare ITO (see SI). Notably, the capacitive character of the junction enables AC applications despite the high DC resistance, which is one of the main novelties of the device presented here. The comparison shows that the SAM together with the intermediate PMMA layer efficiently reduces the contact area between the bottom and the top electrode via the AuNPs and simultaneously defines the distance to the top electrode through which the LSP signal is out-coupled.

Whether the resulting DC resistance of the junction is dominated by the PMMA or the SAM cannot be easily decided. From the asymmetric shape and the very large voltage scale (from  $-5$  to  $+5$  V), we rather attribute it to the properties of PMMA and the interface resistance to the ITO top electrode. The difference between the  $I_{dc}$ – $V_{dc}$  with and without illumination is on the order of 1%, also underlining the negligible contribution of the AuNPs to the DC charge transport properties; see Figure 2a.

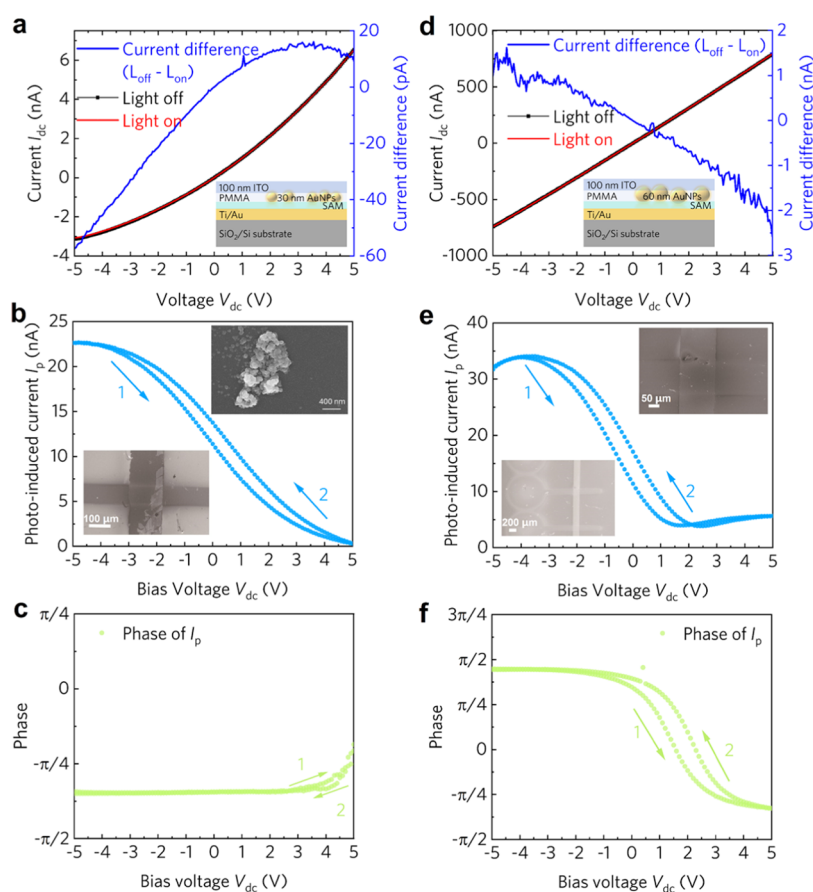


**Figure 3.** Comparison of  $I_{dc}-V_{dc}$  curves and photoinduced current response for different MeMoNPI junctions. The measurement conditions are the same as described in Figure 2. Panels (a–c) represent data recorded on a junction with 30 nm diameter NPs showing aggregation, while panels (d–f) represent data for a junction with 60 nm diameter NPs. (a, d)  $I_{dc}-V_{dc}$  curves measured in the dark (black line) or under continuous illumination (red line) by the semiconductor analyzer. The blue curve represents the current difference between the black and the red curve and refers to the right axis. (b, e) Photoinduced current vs DC offset for the two junctions shown in (a, d). (c, f) Corresponding phase signals to panels (b, e).

Next, we modulate the intensity of laser illumination with 160 kHz and record the AC signal by the LIA under different DC biases to the MeMoNPI junctions. This signal, denoted as photoinduced current  $I_p$ , is large when the shutter is open (red-shaded area in Figure 2b), i.e., the junction is under illumination. When the shutter is closed (laser and modulation frequency always on), no photoinduced current signal can be observed ( $I_p = 0$ ), ruling out electronic cross-talk as an origin of the signal. With illumination, we observe a lock-in voltage in the order of tens of mV, corresponding to currents of tens of nA by virtue of the  $10^6$  transimpedance conversion. We note that the LIA signal corresponds to a change of the current caused by the sine-modulated illumination with the frequency of the LIA modulation and not to the absolute photoinduced DC current flowing in the junction.

We posit that  $I_p$  is determined by the plasmonic, absorptive, and capacitive properties of the junction as modeled by the equivalent RC circuit properties of the device. We can clearly attribute  $I_p$  to arise from LSP excitation in the AuNPs since this signal was absent for the Au-ITO test junctions (see SI, Figure S3d–f). The device's capacitive effects are assumed to be similar to photovoltaic effects in solar cells, where the role of equivalent RC circuits has been studied intensively.<sup>24</sup> The device capacitance is determined by the microcrystalline structure of ITO and by the geometry of the device and can

be estimated to be on the order of a few picofarad. At the modulation frequency of 160 kHz, the AC resistance is on the order of a few M $\Omega$  and hence 2–3 orders of magnitude smaller than the DC resistance. As a result, the photoinduced AC current is 2 to 3 orders larger than the DC current. As the DC bias is scanned from  $-5$  to  $+5$  V, the photoinduced signal, i.e., the modulus of the AC current, first decreases and then undergoes a minimum at around 3 V (Figure 2c). This minimum in the LIA occurs when a phase inversion of  $I_p$  takes place (Figure 2d). These two observations imply that there is a sign change in  $I_p$  at this bias voltage. When inverting the sweep direction, the signal is reversible with a small hysteresis that may arise from the hysteretic capacitive effects of the ITO<sup>26</sup> and reflecting again the capacitive effects of the device being instrumental for the signal shape, marked by the arrows and numbers in Figure 2c,d.

The DC bias-tunability of the photoinduced current signal suggests that it arises from interference between electric field components, at least one of which is related to the bias electric field in the junction. Also this observation can be explained by the rectification effect due to the nonlinear  $I_{dc}-V_{dc}$  characteristics that in one polarity would be adding to the DC electric field, while it would be subtractive for the other DC polarity. Furthermore, the asymmetric geometry of the device breaks the spatial symmetry and may further enhance the asymmetric

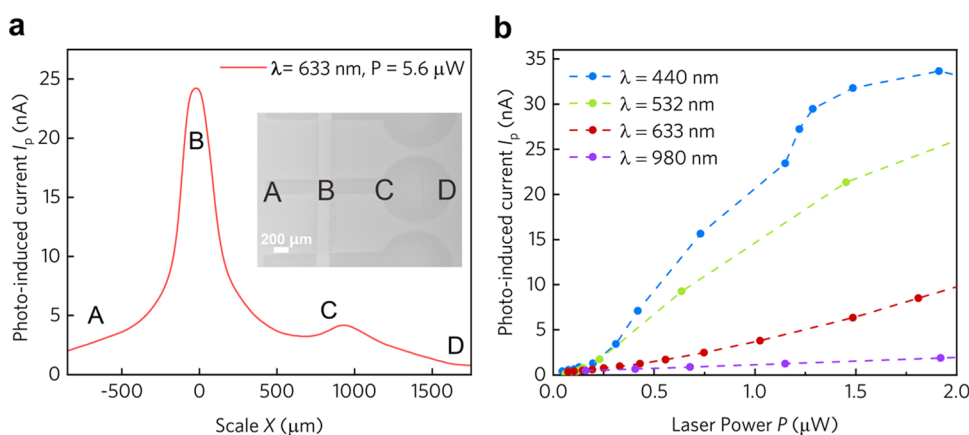


**Figure 4.** Dependence of the photoinduced response on the laser wavelength, intensity, and position. (a) Position-dependent photoinduced current with a laser wavelength of 633 nm and power of 5.6  $\mu\text{W}$  (focused, with a light spot size of  $\sim 50 \mu\text{m}$ ). (b) Corresponding photoinduced current versus optical wavelength and light intensity on the junction for the wavelengths of 440, 532, 633, and 980 nm.

optoelectronic properties, as observed, e.g., in junctions taking advantage of the Schottky diode effect.<sup>27</sup>

To further reveal the origin of this signal, we performed a parameter variation. In Figure 3, we present for comparison data recorded on two samples with different structures, namely, one with 30 nm particles that are partially aggregated [panels (a–c)] and one with isolated particles but 60 nm diameter [panels (d–f)], but identical measurement conditions as used for Figure 2. The sample in Figure 3a–c has been fabricated following the same protocol as the sample from Figure 2, except for the NP self-assembly time that has been increased to 1 h to obtain obvious aggregation. As Figure 3a,b show, the imposed bias enhances (by negative voltages) or reduces (by positive voltages) the photoinduced signals. The  $I_{\text{dc}}-V_{\text{dc}}$  curve in Figure 3a is similar in overall shape as the one shown in Figure 2a, but the photoinduced current difference differs markedly in functional shape. The same holds true for the DC bias dependence of  $I_{\text{p}}$  shown in Figure 3b. The first difference to observe is the disappearance of the sign change of  $I_{\text{p}}$ . As confirmed by the phase information shown in Figure 3c, the bias voltage for the sign change is extrapolated to be slightly larger than 5 V. A possible explanation for this shift of the reversal point to higher bias is the strength of the electric fields arising from LSPs of the NP aggregates, which seem to be stronger than the ones without aggregation. A possible explanation for stronger fields might be the existence of very small gaps between the NPs that are known to give rise to sizable enhancement effects.<sup>28</sup> In view of the proposed counteraction between the LSP fields and the DC bias, the stronger fields of the aggregates require stronger DC fields to be suppressed.

We further selected a junction containing 60 nm diameter NPs while all other conditions are the same compared to the data shown in Figure 2. This junction shows an almost linear  $I_{\text{dc}}-V_{\text{dc}}$  characteristic (Figure 3d) and a 2 order of magnitude lower DC resistance than the junctions with the small NPs. We attribute this difference to the fact that achieving partially exposed NPs by dry etching and hence ohmic contact with the ITO top electrode is easier for larger NPs. In turn, the difference between the DC signal with and without illumination is much smaller since the curvature of the  $I_{\text{dc}}-V_{\text{dc}}$  is much smaller. As a result of these two counteracting influences, increased DC current level, but reduced photoinduced effects, the resulting  $I_{\text{p}}$  has a similar absolute size to

the one from the junctions with smaller NPs. Now, the phase shift occurs already at a DC bias voltage of around 1.5 to 2.5 V. This indicates that in this junction the LSP-induced field is smaller and can therefore be compensated by the DC bias field more easily. This observation is consistent with the smaller field enhancement for larger NP size.<sup>29</sup> The particle density and the coverage in both devices are comparable, which indicates that the light absorption is not the key aspect for the different behavior. The origin of the nonmonotonous behavior at large negative  $V_{\text{dc}}$  is unclear by now. Since the phase remains constant in that bias range with a value expected for purely capacitive currents, we conjecture that here the device performance becomes limited by heating effects due to the high absolute current level. Further experiments are necessary to clarify this aspect.

Notably, the ability to modulate and totally suppress the AC signal by varying the DC bias makes it utilizable as a DC-tunable and AC-signal-transmitting photosensor. Summarizing, the comparative study of several junctions shows that the device properties depend on the microscopic structure of the junction. The shape and reversal position in the  $I_{\text{p}}(V_{\text{DC}})$ -curve reflect the influence of the NP size, the degree of NP aggregation, and electrical conductance arising from the sample's interface properties. NP aggregation enhances the LSP contribution to the total signal, revealing near-field coupling between neighboring NPs. The comparison of these three exemplary devices and others (not shown) reflects that the NP density and the contact quality with the electrodes influence the generation and properties of  $I_{\text{p}}$ . A more quantitative explanation would require the direct confirmation of the microstructure of the devices and their interfaces, especially considering the junction scale of tens of thousands square micrometers.

Apart from the DC bias dependence, we also study the dependence on the illumination position, the light wavelength, and the laser power intensity, while no DC bias is applied to the junction under the same modulation conditions as before. Figure 4a shows the position dependence of the photoinduced current by sweeping the focused laser spot ( $\sim 50 \mu\text{m}$  diameter) with 633 nm wavelength at 5.6  $\mu\text{W}$ , along the top electrode from position A to D for a sample with 30 nm AuNPs without aggregates (see inset in Figure 4a). The highest signal is observed at the exact position of the junction (position B). From there, the signal decays symmetrically around the

junction area. Here, the laser power was chosen at a value such that the maximal response is obtained, as we explain below. The position dependence proves that the signal originates from the junction containing the SAM and the AuNPs and supports our hypothesis that it indicates the plasmonic response of the AuNPs. The small maximum at position C, that is, at the connection of the pad and the lead might be related to a change in the reflection condition of the injected light. Similar phenomena but different intensities of photoinduced current have been observed for laser wavelengths of 440, 532, and 980 nm, see Figure S5. We also did the same position-dependent measurements on the junction containing NP aggregates from Figure 3a–c. The position dependence of the photoinduced current is reproducible for both 633 and 532 nm. The only difference is the observation of a ridge labeled by arrows in Figure S6a, which emerges at the position of high aggregation.

Finally, we investigate the power dependences for these four light wavelengths. We first observe a roughly linear increase of  $I_p$  for all wavelengths. The linearly increasing signal for small power is expected for the rectification effect for  $I_{dc}-V_{dc}$ 's with constant curvature based on the circuit shown in Figure S1g. The slope of the linear increase, corresponding to the photoresponsivity, is highest for 440 nm, followed by 532 and 633 nm, and the signal is very weak for 980 nm wavelength. These slopes correspond to photoresponsivities of 23, 16, 6, and 1 nA/ $\mu$ W for these four wavelengths and this junction, which is roughly a factor 1000 larger than reported for the single AuNP devices in Kos et al.<sup>10</sup> and in a typical range for molecular electronic devices.<sup>30</sup> Knowing that the LSP of AuNPs is located around 510–580 nm, depending on the particle size and dielectric environment,<sup>29,31</sup> one might have expected the highest photoresponsivity for 532 nm. However, also the absorption of the AuNPs changes over this wavelength range.<sup>32</sup> A possible interpretation of the observed wavelength dependence is hence that it is a combination of field enhancement and wavelength dependence of the absorption.<sup>29</sup> Furthermore, when further increasing the power, the signal flattens and eventually reaches a maximum with a similar absolute height of  $I_{p,max} \sim 30$  nA for 440, 532, and 633 nm and much smaller size ( $\sim 3$  nA) for 980 nm. This means that the total photoinduced current is almost independent of the wavelength; it just appears at smaller irradiation power for a shorter wavelength. At very large irradiation power, the signal vanishes for all wavelengths. We verified that the power dependence is reproducible, conforming that the vanishing of the signal is not due to damage. In the Supporting Information, we show a more detailed power dependence recorded with a slightly optically different beam of the junction recorded roughly 18 months later than the initial measurements were performed and find qualitatively equal but slightly smaller values (see Figure S7). This confirms that the presented novel device may serve as a very sensitive and robust photodetector over a wide wavelength range. A tentative explanation of the appearance of the maximum is given in the Supporting Information as well.

## CONCLUSIONS

In conclusion, we successfully fabricated microscale composite junctions by combining 30 or 60 nm diameter plasmonic AuNPs with a transparent ITO top electrode for exciting and characterizing LSP effects and for application in AC optoelectronics. A photoinduced current response is obtained. The four most important observations are as follows: (1) In all

of our measurements, an incident visible light illumination generates an AC current of tens of nanoamperes in one individual junction. We attribute this signal to the LSPs of the AuNPs in connection with the capacitive electrical properties of the devices. (2) We suggest and discuss a possible mechanism for the behavior of the photoinduced signal as a function of sample and measurement parameters. (3) When applying a DC bias to the junction, the photoinduced current response of LSP shows a hysteretic behavior related to the capacitive component in the equivalent RC circuit of the junction. In particular, the photoinduced current of the LSP field can be reversed by applying an appropriate DC bias voltage, and the photoinduced signal can thereby be nullified. The reversal voltage depends on the size of NPs and the aggregation in the junction. (4) The wavelength, light intensity, incident position, and DC bias-tuning dependence of the photoinduced current are investigated. These observations and phenomena could build up the investigation basis for revealing the full complexity of the physical mechanisms and pave the way for future multiple control schemes for optically addressable devices.

## ASSOCIATED CONTENT

### Supporting Information

The Supporting Information is available free of charge at <https://pubs.acs.org/doi/10.1021/acs.jpcc.4c01726>.

Details on the sample fabrication, the particle characterization, results of control experiments on a reference sample, STM break junction data on single-molecule junctions, and results of the position-dependent measurements (PDF)

## AUTHOR INFORMATION

### Corresponding Authors

**Dong Xiang** – Institute of Modern Optics and Center of Single-Molecule Sciences, Nankai University, Tianjin Key Laboratory of Micro-Scale Optical Information Science and Technology, 300350 Tianjin, China; Email: [xiangdongde@nankai.edu.cn](mailto:xiangdongde@nankai.edu.cn)

**Fan Yang** – Department of Physics, University of Konstanz, 78457 Konstanz, Germany; Dynamic Precision Micro&Nano Sensing Technology Research Institute, Chongqing, 400030 Chongqing, China; [orcid.org/0000-0002-4213-2517](https://orcid.org/0000-0002-4213-2517); Email: [fan.yang@uni-konstanz.de](mailto:fan.yang@uni-konstanz.de)

**Elke Scheer** – Department of Physics, University of Konstanz, 78457 Konstanz, Germany; [orcid.org/0000-0003-3788-6979](https://orcid.org/0000-0003-3788-6979); Email: [elke.scheer@uni-konstanz.de](mailto:elke.scheer@uni-konstanz.de)

### Authors

**Maoning Wang** – Institute of Modern Optics and Center of Single-Molecule Sciences, Nankai University, Tianjin Key Laboratory of Micro-Scale Optical Information Science and Technology, 300350 Tianjin, China; Department of Physics, University of Konstanz, 78457 Konstanz, Germany; [orcid.org/0000-0003-0160-1548](https://orcid.org/0000-0003-0160-1548)

**Valentin Barth** – Department of Physics, University of Konstanz, 78457 Konstanz, Germany

**Sergii Negir** – Department of Physics, University of Konstanz, 78457 Konstanz, Germany; [orcid.org/0000-0002-4024-5956](https://orcid.org/0000-0002-4024-5956)

**Lukas Holz** – Department of Chemistry, University of Konstanz, 78457 Konstanz, Germany

Thomas Huhn – Department of Chemistry, University of Konstanz, 78457 Konstanz, Germany; [orcid.org/0000-0001-6292-4215](https://orcid.org/0000-0001-6292-4215)

Johannes Boneberg – Department of Physics, University of Konstanz, 78457 Konstanz, Germany

Chenyang Guo – Institute of Modern Optics and Center of Single-Molecule Sciences, Nankai University, Tianjin Key Laboratory of Micro-Scale Optical Information Science and Technology, 300350 Tianjin, China

Mengqi Fu – Department of Physics, University of Konstanz, 78457 Konstanz, Germany; [orcid.org/0000-0002-7942-8514](https://orcid.org/0000-0002-7942-8514)

Paul Leiderer – Department of Physics, University of Konstanz, 78457 Konstanz, Germany; [orcid.org/0000-0002-2999-0816](https://orcid.org/0000-0002-2999-0816)

Complete contact information is available at:  
<https://pubs.acs.org/10.1021/acs.jpcc.4c01726>

### Author Contributions

E.S., F.Y., and D.X. supervised the project. M.W., F.Y., and V. B. designed and performed the experiments. T.H. and L. H. synthesized the molecules and gave advice for the SAM formation. M.W. and F.Y. wrote the manuscript. F.Y., V.B., J.B., P.L., and E.S. analyzed the data. S.S. and D.X. contributed to fruitful discussions. All authors contributed to editing and corrections. E.S., J.B., and P.L. revised the manuscript before the final submission.

### Notes

The authors declare no competing financial interest.

### ACKNOWLEDGMENTS

The authors thank Oluwafemi S. Ojambati and X.Y. Jiang for fruitful discussions and the nano.lab of the University of Konstanz for providing lab access and M. Hagner for advice and training. F. Yang thanks D.L. Hou for help with the art design of the 3D model. This work was supported by the National Key R&D Program of China (2021YFA1200103), the National Natural Science Foundation of China (22273041, 91950116, and 11804170), and the Natural Science Foundation of Tianjin (19JCZDJC31000 and 19JCJQJC60900) as well as by the Deutsche Forschungsgemeinschaft under the Plasmochrom project (project ID 406778771) and SFB 1432 (project ID 425217212). M.W. also held a China Scholarship Council Studentship at the University of Konstanz (202006200069) and was supported by a scholarship from the University of Konstanz.

### REFERENCES

- (1) Chen, H.; Su, L.; Jiang, M.; Fang, X. Highly Desirable Photodetectors Derived from Versatile Plasmonic Nanostructures. *Adv. Funct. Mater.* **2017**, *27*, No. 1704181.
- (2) Hu, K.; Chen, H.; Jiang, M.; Teng, F.; Zheng, L.; Fang, X. Broadband photoresponse enhancement of a high-performance t-Se microtube photodetector by plasmonic metallic nanoparticles. *Adv. Funct. Mater.* **2016**, *26*, 6641–6648.
- (3) Mandal, P.; Tewari, B. S. Progress in surface enhanced Raman scattering molecular sensing: A review. *Surf. Interfaces* **2022**, *28*, No. 101655.
- (4) Ma, R.-M.; Wang, S.-Y. Plasmonic nanolasers: fundamental properties and applications. *Nanophotonics* **2021**, *10*, 3623–3633.
- (5) Zeng, B.-F.; Deng, R.; Zou, Y.-L.; Huo, C.-A.; Wang, J.-Y.; Yang, W.-M.; Liang, Q.-M.; Qiu, S.-J.; Feng, A.; Shi, J.; et al. Optical

Trapping of a Single Molecule of Length Sub-1 nm in Solution. *CCS Chem.* **2023**, *5*, 830–840.

(6) Zhang, X.; Yang, J. Ultrafast Plasmonic Optical Switching Structures and Devices. *Front. Phys.* **2019**, *7*, 190.

(7) Möller, R.; Albrecht, U.; Boneberg, J.; Koslowski, B.; Leiderer, P.; Dransfeld, K. Detection of Surface Plasmons by Scanning Tunneling Microscopy. *J. Vac. Sci. Technol., B* **1991**, *9*, 506–509.

(8) Wang, M.; Wang, T.; Ojambati, O. S.; Duffin, T. J.; Kang, K.; Lee, T.; Scheer, E.; Xiang, D.; Nijhuis, C. A. Plasmonic phenomena in molecular junctions: principles and applications. *Nat. Rev. Chem.* **2022**, *6*, 681–704.

(9) Neutens, P.; Van Dorpe, P.; De Vlamincq, I.; Lagae, L.; Borghs, G. Electrical detection of confined gap plasmons in metal–insulator–metal waveguides. *Nat. Photonics* **2009**, *3*, 283–286.

(10) Kos, D.; Assumpcao, D. R.; Guo, C.; Baumberg, J. J. Quantum tunneling induced optical rectification and plasmon-enhanced photocurrent in nanocavity molecular junctions. *ACS Nano* **2021**, *15*, 14535–14543.

(11) Axelevitch, A.; Gorenstein, B.; Golan, G. Investigation of Optical Transmission in Thin Metal Films. *Phys. Procedia* **2012**, *32*, 1–13.

(12) Al-Zubeidi, A.; McCarthy, L. A.; Rafiei-Miandashti, A.; Heiderscheid, T. S.; Link, S. Single-particle scattering spectroscopy: fundamentals and applications. *Nanophotonics* **2021**, *10*, 1621–1655.

(13) Wang, L. D.; Zhang, T.; Zhu, S. Q.; Zhang, X. Y.; Wang, Q. L.; Liu, X.; Li, R. Z. Two-dimensional ultrathin gold film composed of steadily linked dense nanoparticle with surface plasmon resonance. *Nanoscale Res. Lett.* **2012**, *7*, 683.

(14) Kulkarni, A. K.; Schulz, K. H.; Lim, T. S.; Khan, M. Electrical, optical and structural characteristics of indium-tin-oxide thin films deposited on glass and polymer substrates. *Thin Solid Films.* **1997**, *308–309*, 1–7.

(15) Sofi, A. H.; Shah, M. A.; Asokan, K. Structural, Optical and Electrical Properties of ITO Thin Films. *J. Electron. Mater.* **2018**, *47*, 1344–1352.

(16) Lee, K.-S.; Mo, Y. J.; Park, I. K.; Park, T.-S.; Kim, Y. S. A Study on Transparent Electrode Properties of Indium Tin Oxide Thin Films Deposited From Recycled Target. *Bull. Korean Chem. Soc.* **2020**, *41*, 341–347.

(17) Kim, J.; Shrestha, S.; Souri, M.; Connell, J. G.; Park, S.; Seo, A. High-temperature optical properties of indium tin oxide thin-films. *Sci. Rep.* **2020**, *10*, No. 12486.

(18) Andrés, A.; Jiménez-Villacorta, F.; Prieto, C. *Transparent Conductive Materials*; Levy, D.; Castellon, E., Eds.; Wiley-VCH: Germany, 2018; Vol. 11, pp 1–30.

(19) Tan, J. L.; Tien, J.; Chen, C. S. Microcontact Printing of Proteins on Mixed Self-Assembled Monolayers. *Langmuir* **2002**, *18*, 519–523.

(20) Prime, K. L.; Whitesides, G. M. Adsorption of Proteins onto Surfaces Containing End Attached oligo (ethyleneoxide): A Model System Using Self-Assembled Monolayers. *J. Am. Chem. Soc.* **1993**, *115*, 10714–10721.

(21) Prime, K. L.; Whitesides, G. M. Self-Assembled Organic Monolayers: Model Systems for Studying Adsorption of Proteins at Surfaces. *Science* **1991**, *252*, 1164–1167.

(22) Vilan, A.; Aswal, D.; Cahen, D. Large-Area, Ensemble Molecular Electronics: Motivation and Challenges. *Chem. Rev.* **2017**, *117*, 4248–4286.

(23) Farid, N.; Sharif, A.; Vijayaraghavan, R. K.; Wang, M.; Chan, H.; Brunton, A.; McNally, P. J.; Choy, K. L.; O'Connor, G. M. Improvement of electrical properties of ITO thin films by melt-free ultra-short laser crystallization. *J. Phys. D: Appl. Phys.* **2021**, *54*, No. 185103.

(24) Ravishankar, S.; Riquelme, A.; Sarkar, S. K.; Garcia-Battle, M.; Garcia-Belmonte, G.; Bisquert, J. Intensity-Modulated Photocurrent Spectroscopy and Its Application to Perovskite Solar Cells. *J. Phys. Chem. C* **2019**, *123*, 24995–25014.

(25) Cuevas, J. C.; Scheer, E. *Molecular Electronics: An Introduction to Theory and Experiment*; World Scientific: London, 2017.

(26) Won, S. J.; Huh, M. S.; Park, S.; Suh, S.; Park, T. J.; Kim, J. H.; Hwang, C. S.; Kim, H. J. Capacitance and interface analysis of transparent analog capacitor using indium tin oxide electrodes and high-k dielectrics. *J. Electrochem. Soc.* **2010**, *157*, G170.

(27) Clavero, C. Plasmon-induced hot-electron generation at nanoparticle/metal-oxide interfaces for photovoltaic and photocatalytic devices. *Nat. Photonics* **2014**, *8*, 95–103.

(28) Kumari, G.; Kandula, J.; Narayana, C. How Far Can We Probe by SERS? *J. Phys. Chem. C* **2015**, *119*, 20057.

(29) Sun, A. Y.; Lee, Y. C.; Chang, S. W.; Chen, S. L.; Wang, H. C.; Wan, D.; Chen, H. L. Diverse substrate-mediated local electric field enhancement of metal nanoparticles for nanogap-enhanced Raman scattering. *Anal. Chem.* **2021**, *93*, 4299–4307.

(30) Yang, J.; Li, J.; Bahrami, A.; Nasiri, N.; Lehmann, S.; Cichocka, M. O.; Mukherjee, S.; Nielsch, K. Wafer-scale growth of Sb<sub>2</sub>Te<sub>3</sub> films via low-temperature atomic layer deposition for self-powered photodetectors. *ACS Appl. Mater. Interfaces* **2022**, *14*, 54034–54043.

(31) Louis, C.; Pluchery, O. *Gold Nanoparticles for Physics, Chemistry and Biology*; World Scientific: London, 2017.

(32) Amendola, V.; Pilot, R.; Frasconi, M.; Maragò, O. M.; Iati, M. A. Surface plasmon resonance in gold nanoparticles: a review. *J. Phys.: Condens. Matter* **2017**, *29*, No. 203002.